

# High-resolution X-ray spectroscopy reveals the special nature of Wolf-Rayet star winds

L.M. Oskinova

*Institute for Physics and Astronomy, University Potsdam, 14476 Potsdam, Germany*

`lida@astro.physik.uni-potsdam.de`

K.G. Gayley

*Department of Physics and Astronomy, University of Iowa, Iowa City, IA 52245, USA*

W.-R. Hamann

*Institute for Physics and Astronomy, University Potsdam, 14476 Potsdam, Germany*

D.P. Huenemoerder

*Massachusetts Institute of Technology, Kavli Institute for Astrophysics and Space Research,  
70 Vassar St., Cambridge, MA 02139, USA*

R. Ignace

*Department of Physics and Astronomy, East Tennessee State University, Johnson City,  
TN 37663, USA*

A.M.T. Pollock

*European Space Agency XMM-Newton Science Operations Centre, European Space  
Astronomy Centre, Apartado 78, Villanueva de la Cañada, 28691 Madrid, Spain*

## ABSTRACT

We present the first high-resolution X-ray spectrum of a putatively single Wolf-Rayet star. 400 ks observations of WR6 by the XMM-*Newton*-telescope resulted in a superb quality high-resolution X-ray spectrum. Spectral analysis reveals that the X-rays originate far out in the stellar wind, more than 30 stellar radii from the photosphere, and thus outside the wind acceleration zone where the line-driving instability could create shocks. The X-ray emitting plasma reaches temperatures up to 50 MK, and is embedded within the un-shocked, “cool” stellar wind as revealed by characteristic spectral signatures. We detect a fluorescent Fe

line at  $\approx 6.4$  keV. The presence of fluorescence is consistent with a two-component medium, where the cool wind is permeated with the hot X-ray emitting plasma. The wind must have a very porous structure to allow the observed amount of X-rays to escape. We find that neither the line-driving instability nor any alternative binary scenario can explain the data. We suggest a scenario where X-rays are produced when the fast wind rams into slow "sticky clumps" that resist acceleration. Our new data show that the X-rays in single WR-star are generated by some special mechanism different from the one operating in the O-star winds.

*Subject headings:* Stars: winds, outflows — Stars: Wolf-Rayet — Stars: individual: WR 6 — X-rays: stars

## 1. Introduction

Massive stars reach the Wolf-Rayet (WR) evolutionary phase when their hydrogen fuel has been consumed or lost and the products of nuclear fusion appear in their atmospheres, before ending their short lives among the progenitors of core-collapse supernovae (SNe) (Smartt 2009). These stars are millions of times more luminous than the sun and drive strong stellar winds by radiation pressure exerted through absorption and scattering in spectral lines (Nugis & Lamers 2002; Gräfener & Hamann 2005). This "line-driving" mechanism is known to be unstable (Lucy & White 1980) and is thought to create hydrodynamic shocks that heat the plasma to a few million degrees with the emission of thermal X-rays (Feldmeier et al. 1997). For O-type stars, which have weaker winds than WR stars, this model is largely consistent with the observations (Oskinova et al. 2006; Güdel & Nazé 2009). The winds of WR stars are also expected to suffer from the line-driving instability (LDI) (Gayley & Owocki 1995) and thus may emit X-rays similar to the O-type stars. This conjecture was not verified by observations so far.

In this *Letter* we report the first high-resolution X-ray spectrum of a putatively single WN-type star and its analysis.

## 2. The WN star WR 6

The object of our study, WR 6 (EZ CMa, HD 50896), has been successfully modeled as a hydrogen-free WN star of subtype WN5 by fitting its UV, visible, and infrared spectra (Hamann et al. 2006). Its stellar temperature is 90 kK, and its luminosity is  $10^{5.6} L_{\odot}$  when adopting a distance of 1.82 kpc as implied from its membership to the association

Collinder 121. The mass-loss rate is  $\dot{M} \approx 2 \times 10^{-5} M_{\odot} \text{ yr}^{-1}$ , and the wind reaches a terminal velocity of  $v_{\infty} \approx 1,700 \text{ km s}^{-1}$ . Hence the wind carries a mechanical power  $\dot{M}v_{\infty}^2/2$  equivalent to  $10^4 L_{\odot}$ , which is about 3% of the stellar luminosity.

The WR winds are strongly inhomogeneous (Lépine & Moffat 1999). Narrow spectral features drifting over the broad emission-line profiles are interpreted as showing radially accelerated blobs of matter (Moffat et al. 1988). Quasi-periodic variability could be related to rotation (Dessart & Chesneau 2002) and caused by spiral-like density patterns in the wind rooted in the photosphere, similar to the corotating interaction regions observed in the solar wind (Mullan 1984; Morel et al. 1997). WR 6 shows considerable photometric, spectral, and polarimetric variability on the time scale of 3.766 d (Duijsens et al. 1996; St-Louis et al. 2009).

Its thermal radio spectrum (Dougherty & Williams 2000) and complex variability pattern (Duijsens et al. 1996) support the conclusion that WR 6 is not a binary but a single star. Previous X-ray observations of WR 6 at lower spectral resolution confirmed that its X-ray luminosity and temperature are typical of single WN stars (Pollock 1987; Ignace et al. 2003; Oskinova 2005; Skinner et al. 2010).

### 3. Observations and Spectral Modeling

The X-ray data on WR 6 were taken with the X-Ray Multi-Mirror Satellite *XMM-Newton*. Its telescopes illuminate three different instruments which always operate simultaneously: RGS is a Reflection Grating Spectrometer, achieving a spectral resolution of  $0.07 \text{ \AA}$ ; RGS is not sensitive for wavelengths shorter than  $5 \text{ \AA}$ . The other focal instruments MOS and PN cover the shorter wavelengths; their spectral resolution is modest ( $E/\Delta E \approx 20 - 50$ ).

The data were obtained at four epochs in 2010 (Oct. 11 and 13, Nov. 4 and 6). The total exposure time of 400 kilosecond was split into four individual parts. Our data reduction involved standard procedures of the *XMM-Newton* Science Analysis System v.10.0.

The RGS spectrum is shown in Fig. 1. The X-ray luminosity of WR 6 in the  $0.3 - 12.0 \text{ keV}$  band is  $L_X \approx 8 \times 10^{32} \text{ erg s}^{-1}$ , or  $0.1 L_{\odot}$ . This constitutes  $10^{-5}$  of the wind's mechanical power. The RGS spectrum is dominated by strong and broad emission lines of metals in accordance with the WN-wind abundances characteristic of CNO processed material.

To model the observed X-ray spectrum we generated emissivities for a hydrogen-free plasma with the APEC thermal plasma model (Smith et al. 2001). For most elements the

abundances were fixed to the values derived from the UV and optical spectra.

In this stage we approximate the line profiles by Gaussians, with a common Doppler shift against the laboratory wavelength of  $-650 \text{ km s}^{-1}$  and a width (FWHM) of  $3000 \text{ km s}^{-1}$  as the best values found by the automatic procedure from fitting the RGS data. The optimum fits to the observed spectra were obtained with the ISIS software (Noble & Nowak 2008).

The observed spectra, the best-fitting model, and the residuals are shown in Fig. 2. In order to achieve an acceptable fit, it was necessary to compose the emission from plasmas of three different temperatures (1.6, 7.0 and 45 MK) with respective emission measures of 253, 86, and  $22 \times 10^{54} \text{ cm}^{-3}$ . The hottest component is required to reproduce the 2–5 Å continuum and the emission lines from Fe xxv, Ca xix, Ar xvii, and S xv. Nevertheless, there are still residuals at some lines, such as Mg xii and Ne x, indicating that a three-temperature model is not fully sufficient, or that some abundances are not well determined. O and C lines are absent or very weak, as expected for a plasma with the chemical composition of a WN-type wind.

To account for the absorption within the wind we applied the *vphabs* model (Arnaud 1996), modified for the absence of hydrogen. Strong absorption, significantly exceeding that of the interstellar medium towards the star, is evident. The ratio of fluxes in the N vi and N vii Ly $\alpha$  lines is reproduced when absorption in the cool wind is included, especially the K-shell ionization edge of N iv that is located between the two aforementioned lines (see Fig 2).

The low-resolution EPIC spectra provide data up to 12 keV. Significant residuals are encountered in the region around the Fe xxv line at about 1.9 Å (see Fig. 2). The observation shows a definitely broader feature than reproduced by the plasma model. Obviously, this complex includes a further blend. The fit of an additional gaussian profile yields a flux of  $4.5 \times 10^{-7} \text{ photons cm}^{-2} \text{ s}^{-1}$  and a line center at 1.92 Å. The latter value agrees within the uncertainties with the wavelength of the Fe K $\alpha$  line (1.94 Å). Hence we conclude that cool-wind material must be irradiated by X-rays which are hard enough ( $> 7.1 \text{ keV}$ ) to excite this line by fluorescence. Our PoWR wind models show that in the outer wind the leading ionization stage of iron is Fe v. The presence of fluorescence is consistent with a two-component medium, where the cool wind is permeated with the hot X-ray emitting plasma.

#### 4. The cool wind model of WR 6

To determine the physical conditions in the “cool” component of the stellar wind, we employ the PoWR model atmosphere code (Hamann & Gräfener 2004). The PoWR code solves the non-LTE radiative transfer simultaneously with the equations of statistical and radiative equilibrium. Complex model atoms with thousands of transitions are taken into account. The extensive inclusion of the iron group elements is important because of their blanketing effect on the atmospheric structure (Gräfener et al. 2002). A particular stellar atmosphere model is defined by the effective temperature, surface gravity, luminosity, mass-loss rate, wind terminal velocity, and chemical composition.

For the supersonic part of the wind, we adopt the radial dependence of velocity as  $v(r) = v_\infty(1 - 1/r)$ , where  $r$  is in units of the stellar radius  $R_*$ , and the terminal velocity  $v_\infty$  is a free parameter. In the subsonic region, the velocity field is defined such that the hydrostatic density stratification is approached. The PoWR models account for stellar-wind clumping in the standard volume-filling factor ‘microclumping’ approximation (Hillier 1991; Hamann & Koesterke 1998). Our best model of WR 6 has a clumping factor  $D = 20$ , where  $D = \langle \rho^2 \rangle / \langle \rho \rangle^2$ . The synthetic spectra are calculated over the whole spectral range from UV to IR, and then compared to the observed spectra and photometric fluxes.

With the final wind model being adopted, the stratifications of the density, opacity, ionization, and radiative flux are defined. The mass absorption increases with distance from the star, partly because the fully ionized helium recombines to He II with its strong bound-free opacity. This increase of the mass absorption coefficient partly compensates for the decrease of matter density, keeping the wind opaque to large radii.

In Fig. 3 (upper panel) we show the radius in the wind where the continuum optical depth on the radial ray becomes unity, as predicted by PoWR model. Roughly speaking, only X-rays emitted from outside that radius can escape from the wind and be seen by a distant observer, unless inhomogeneities create some porosity (“macroclumping”).

#### 5. The analysis of line ratios in He-like ions

Helium-like ions show a group of three lines, consisting of a forbidden ( $f$ ), an intercombination ( $i$ ), and a resonance ( $r$ ) transition – the so-called *fir* triplet. The *fir* triplets of Si XIII, Mg XI, Ne IX, and N VI are present in the RGS spectrum of WR 6. As illustrated in Fig. 4, the line ratios observed in WR 6 are very different from those observed in typical single O-type stars. For N VI the ratio  $f/i$  exceeds unity in WR 6, while O stars show  $f/i < 1$  (Leutenegger et al. 2006; Waldron & Cassinelli 2007).

For each He-like ion, the ratio of fluxes between the forbidden and the intercombination component,  $R$ , is sensitive to the electron density and the ultraviolet flux (Blumenthal et al. 1972):

$$R(r) = \frac{\mathcal{R}_0}{1 + \phi(r)/\phi_c + N_e(r)/N_c}, \quad (1)$$

where  $\phi$  is the photoexcitation rate from the term  $2s^3S$  to  $2p^3P$ , and  $N_e$  is the electron density. The quantities  $\mathcal{R}_0$ ,  $\phi_c$ , and  $N_c$  depend only on atomic parameters and the electron temperature (Blumenthal et al. 1972; Porquet et al. 2001).

We use the PoWR model to calculate the values of  $R(r)$  for Mg XI, Ne IX, and N VI as function of the radial location in the wind of WR 6. The density in the X-ray emitting shocks is not known, therefore we computed two sets of  $R(r)$ , one neglecting the density term, and another one assuming that the density in the shock is the same as in the ambient “cool” wind but the plasma is fully ionized. According to the strong-shock condition, the hot gas density would be even a factor of four higher than that (Zeldovich & Raizer 1966). The photo-excitation rates  $\phi(r)$  are computed at each radius from the radiation intensity as provided by the PoWR model, which accounts not only simply for geometric dilution, but also for the diffuse radiative field. Fig. 3 (low panel) shows for the N VI triplet the predicted  $R$  ratio as function of the radial location of the emitting plasma with the best-fit value of  $\approx 200 R_*$  when the collisions are accounted for. The N VI emission line indicates a plasma temperature of  $\approx 1.58$  MK, which could be reached in a strong shock with a velocity jump by  $\approx 400 \text{ km s}^{-1}$ .

## 6. Modeling of X-ray emission line profiles

The broadening of the X-ray lines from WR 6 is consistent with the known terminal velocity of the wind of  $\approx 1700 \text{ km s}^{-1}$ . The lines centers are displaced from their laboratory wavelengths by  $\approx -0.06 \text{ \AA}$  (see Fig. 5). Such blue-shifts are predicted if the line emission is distributed within a partly absorbing wind (e.g. Macfarlane et al. 1991; Ignace 2001). However, according to the standard model, the wind of WR 6 remains optically thick till large distances from the star ( $550 - 900 R_*$  for  $\lambda > 20 \text{ \AA}$ ). X-rays can hardly emerge from interior to this location unless the wind is very porous.

We employed our 2-D stochastic wind code (Oskinova et al. 2004) to model the observed X-ray lines. Relaxing the microclumping approximation, the clumps may have arbitrary optical depth (“macroclumping”). This wind fragmentation alters the radiative transfer drastically, compared to a homogeneous wind with the same mass-loss rate (Feldmeier et al. 2003). The X-rays can escape from deeper in the wind than indicated in the upper panel in

Fig. 3 for the smooth-wind model.

We assume that parcels of X-ray emitting gas are distributed between clumps of continuum-absorbing, cool wind. The wind is fully fragmented throughout the whole relevant radial range. The X-ray emission is placed only at radii larger than  $r_{\text{em}}$ . Since thermal X-ray emission arises from the decay of collisionally excited levels and from free-free emission, is plausible to assume that the emissivity scales as the square of the density,  $\eta_{\lambda} \propto \rho^2$ . With this scaling, most X-rays are released close to  $r_{\text{em}}$ . The intensity along any ray is reduced by the factor  $\exp(-\tau_{\lambda}^c)$ , where  $\tau_{\lambda}^c$  is the summation over the optical depths through all individual clumps which are encountered.

A grid of line models was calculated for different values of the radius  $r_{\text{em}}$  and  $\langle N_c \rangle$  – the time-averaged number of fragments in a radial direction. The radial dependence of the mass-absorption coefficient and the wind opacity was accounted for in the models. Even with porosity, emission arising from too close to the star is totally trapped, while the adopted scaling of the emissivity with  $\rho^2$  requires an unrealistic amount of energy being converted into X-rays. This excludes small values of  $r_{\text{em}}$ . In the other extreme, when X-ray emission starts only at radii where the wind is already nearly transparent, the observed blue-shift and asymmetry of the line profiles cannot be reproduced. The model line profiles shown in Fig. 5 were calculated with  $r_{\text{em}} = 30 R_*$  and  $\langle N_c \rangle = 50$ .

## 7. On The Origin of X-ray Emission in WR stars

Observed temperatures up to 50 MK require shock velocity jumps comparable to the wind speed. From UV spectra of WR6 there is direct evidence that a fraction of the wind flows with much higher velocity (up to  $3,100 \text{ km s}^{-1}$ ) than the general wind speed ( $1,700 \text{ km s}^{-1}$ ) (Prinja et al. 1990). We suggest that the hottest gas is produced when very fast flows impacts on slowly moving clumps within the wind acceleration zone. Such extreme shocks cannot be maintained to large radii, but the hardest X-rays can escape from the inner wind owing to smaller absorption cross-sections at higher energies.

Exceptionally large, pancake-shaped clumps which form close to the photosphere at low velocities would resist the radiative acceleration. Being an obstacle to the generally much faster wind, they create strong reverse shocks that may add more mass to the clump if the gas cools quickly, or generate bow shocks if it does not (Cassinelli et al. 2008). Self-consistent kinematic models of Gayley (in prep.) show that  $500 \text{ km s}^{-1}$  shocks may be present at  $\sim 50 R_*$  in the wind, suitable for X-ray escape if the wind is sufficiently porous.

## 8. On the binary hypothesis for WR 6

The X-ray emission of WR 6 varies considerably (Pollock 1987; Willis & Stevens 1996). Our new observations confirm and extend these results. The XMM-*Newton* light curve shows different variability time scales, including a variation of 20% over a month’s span. We also observe some spectral changes. The X-ray variability does not follow the 3.766 d period which is seen in the optical and UV (Willis et al. 1989). The X-ray variability of WR 6 further highlights the differences between single WR and O stars. The latter are remarkably constant X-ray sources (Nazé et al. 2012, submitted).

The optical variability of WR 6 has long been known (Wilson 1948), and it appears to be incompatible with stellar pulsations or the Be star phenomenology (Robert et al. 1992). Most plausibly, the variability is due to changes of wind structures (St.-Louis et al. 1993; Flores et al. 2011). This explanation is in line with our new X-ray observations.

Firmani et al. (1980) established that if the 3.766 day period were associated with binarity, the mass of the secondary star could not be larger than  $\approx 1.5 M_{\odot}$ . A star of such mass and age (assuming coeval formation of both binary components) would be either a degenerate neutron star (NS) or a pre main-sequence young stellar object (T Tauri type star).

The NS scenario was criticized because of the relatively low X-ray luminosity of WR 6 and the lack of evidence in its UV spectrum (Stevens & Willis 1988). The WR+T Tau scenario is also extremely unlikely, as the high-resolution X-ray spectrum of WR 6 is incompatible with the X-ray properties of young stellar objects (Kastner et al. 2002).

Variability is a common property of WR stars. Among rigorously monitored WN stars, 40% show optical variability similar to WR 6 (Chené & St-Louis 2011). The assumption that 40% of all WN stars have a NS or a T Tauri type companion is not realistic.

Our high-resolution X-ray spectra show that the X-ray emitting plasma moves at about the same velocity as the cool wind. The X-ray line blue-shifts do apparently not change with time. The X-ray emission line spectrum is compatible with the WN star abundances. All these facts add further evidence against WR 6 being a binary system.

## 9. Conclusions

Assuming that WR 6 is typical, our results show that in the winds of WN stars strong shocks are active at large radii from stellar photosphere. A possible explanation involves slow, dense clumps that accumulate from the wind close above the photosphere without being ef-



fectively accelerated. The seeding of such slow clumps might be associated with (sub)surface convective zones (Cantiello & Braithwaite 2011). The effects of such wind anisotropies on the distribution of circumstellar matter could influence the behavior of SN Ibc.

In any case, from high-resolution X-ray spectral data of WR 6 we conclude that unknown mechanisms must operate in WR winds. Identifying these mechanisms poses a challenging problem for the theory of stellar winds.

Based on observations made with *XMM-Newton*, an ESA science mission with instruments and contributions directly funded by ESA member states and the USA (NASA). We thank R.K. Smith and A. Foster for help in computing emissivities for a hydrogen-depleted plasma. DPH was supported by NASA through the Smithsonian Astrophysical Observatory contract SV3-73016 for the Chandra X-Ray Center and Science Instruments. Funding for this research has been provided by DLR grant 50 OR 1101 (LMO).

## REFERENCES

- Arnaud, K. A. 1996, in *Astronomical Society of the Pacific Conference Series*, Vol. 101, *Astronomical Data Analysis Software and Systems V*, ed. G. H. Jacoby & J. Barnes, 17–+
- Blumenthal, G. R., Drake, G. W. F., & Tucker, W. H. 1972, *ApJ*, 172, 205
- Cantiello, M., & Braithwaite, J. 2011, *A&A*, 534, A140
- Cassinelli, J. P., Ignace, R., Waldron, W. L., et al. 2008, *ApJ*, 683, 1052
- Chené, A.-N., & St-Louis, N. 2011, *ApJ*, 736, 140
- Dessart, L., & Chesneau, O. 2002, *A&A*, 395, 209
- Dougherty, S. M., & Williams, P. M. 2000, *MNRAS*, 319, 1005
- Duijsens, M. F. J., van der Hucht, K. A., van Genderen, A. M., et al. 1996, *A&AS*, 119, 37
- Feldmeier, A., Oskinova, L., & Hamann, W.-R. 2003, *A&A*, 403, 217
- Feldmeier, A., Puls, J., & Pauldrach, A. W. A. 1997, *A&A*, 322, 878
- Firmani, C., Koenigsberger, G., Bisiacchi, G. F., Moffat, A. F. J., & Isserstedt, J. 1980, *ApJ*, 239, 607

- Flores, A., Koenigsberger, G., Cardona, O., & de La Cruz, L. 2011, *Rev. Mexicana Astron. Astrofis.*, 47, 261
- Gayley, K. G., & Owocki, S. P. 1995, *ApJ*, 446, 801
- Gräfener, G., & Hamann, W.-R. 2005, *A&A*, 432, 633
- Gräfener, G., Koesterke, L., & Hamann, W.-R. 2002, *A&A*, 387, 244
- Güdel, M., & Nazé, Y. 2009, *A&A Rev.*, 17, 309
- Hamann, W.-R., & Gräfener, G. 2004, *A&A*, 427, 697
- Hamann, W.-R., Gräfener, G., & Liermann, A. 2006, *A&A*, 457, 1015
- Hamann, W.-R., & Koesterke, L. 1998, *A&A*, 335, 1003
- Hillier, D. J. 1991, *A&A*, 247, 455
- Ignace, R. 2001, *ApJ*, 549, L119
- Ignace, R., Oskinova, L. M., & Brown, J. C. 2003, *A&A*, 408, 353
- Kastner, J. H., Huenemoerder, D. P., Schulz, N. S., Canizares, C. R., & Weintraub, D. A. 2002, *ApJ*, 567, 434
- Lépine, S., & Moffat, A. F. J. 1999, *ApJ*, 514, 909
- Leutenegger, M. A., Paerels, F. B. S., Kahn, S. M., & Cohen, D. H. 2006, *ApJ*, 650, 1096
- Lucy, L. B., & White, R. L. 1980, *ApJ*, 241, 300
- Macfarlane, J. J., Cassinelli, J. P., Welsh, B. Y., et al. 1991, *ApJ*, 380, 564
- Moffat, A. F. J., Drissen, L., Lamontagne, R., & Robert, C. 1988, *ApJ*, 334, 1038
- Morel, T., St-Louis, N., & Marchenko, S. V. 1997, *ApJ*, 482, 470
- Mullan, D. J. 1984, *ApJ*, 283, 303
- Noble, M. S., & Nowak, M. A. 2008, *PASP*, 120, 821
- Nugis, T., & Lamers, H. J. G. L. M. 2002, *A&A*, 389, 162
- Oskinova, L. M. 2005, *MNRAS*, 361, 679
- Oskinova, L. M., Feldmeier, A., & Hamann, W.-R. 2004, *A&A*, 422, 675

- . 2006, MNRAS, 372, 313
- Pollock, A. M. T. 1987, ApJ, 320, 283
- Porquet, D., Mewe, R., Dubau, J., Raassen, A. J. J., & Kaastra, J. S. 2001, A&A, 376, 1113
- Prinja, R. K., Barlow, M. J., & Howarth, I. D. 1990, ApJ, 361, 607
- Robert, C., Moffat, A. F. J., Drissen, L., et al. 1992, ApJ, 397, 277
- Skinner, S. L., Zhekov, S. A., Güdel, M., Schmutz, W., & Sokal, K. R. 2010, AJ, 139, 825
- Smartt, S. J. 2009, ARA&A, 47, 63
- Smith, R. K., Brickhouse, N. S., Liedahl, D. A., & Raymond, J. C. 2001, ApJ, 556, L91
- St-Louis, N., Chené, A.-N., Schnurr, O., & Nicol, M.-H. 2009, ApJ, 698, 1951
- St.-Louis, N., Howarth, I. D., Willis, A. J., et al. 1993, A&A, 267, 447
- Stevens, I. R., & Willis, A. J. 1988, MNRAS, 234, 783
- Waldron, W. L., & Cassinelli, J. P. 2007, ApJ, 668, 456
- Willis, A. J., Howarth, I. D., Smith, L. J., Garmany, C. D., & Conti, P. S. 1989, A&AS, 77, 269
- Willis, A. J., & Stevens, I. R. 1996, A&A, 310, 577
- Wilson, O. C. 1948, PASP, 60, 383
- Zeldovich, Y. B., & Raizer, Y. P. 1966, Elements of gasdynamics and the classical theory of shock waves, ed. Zeldovich, Y. B. & Raizer, Y. P.

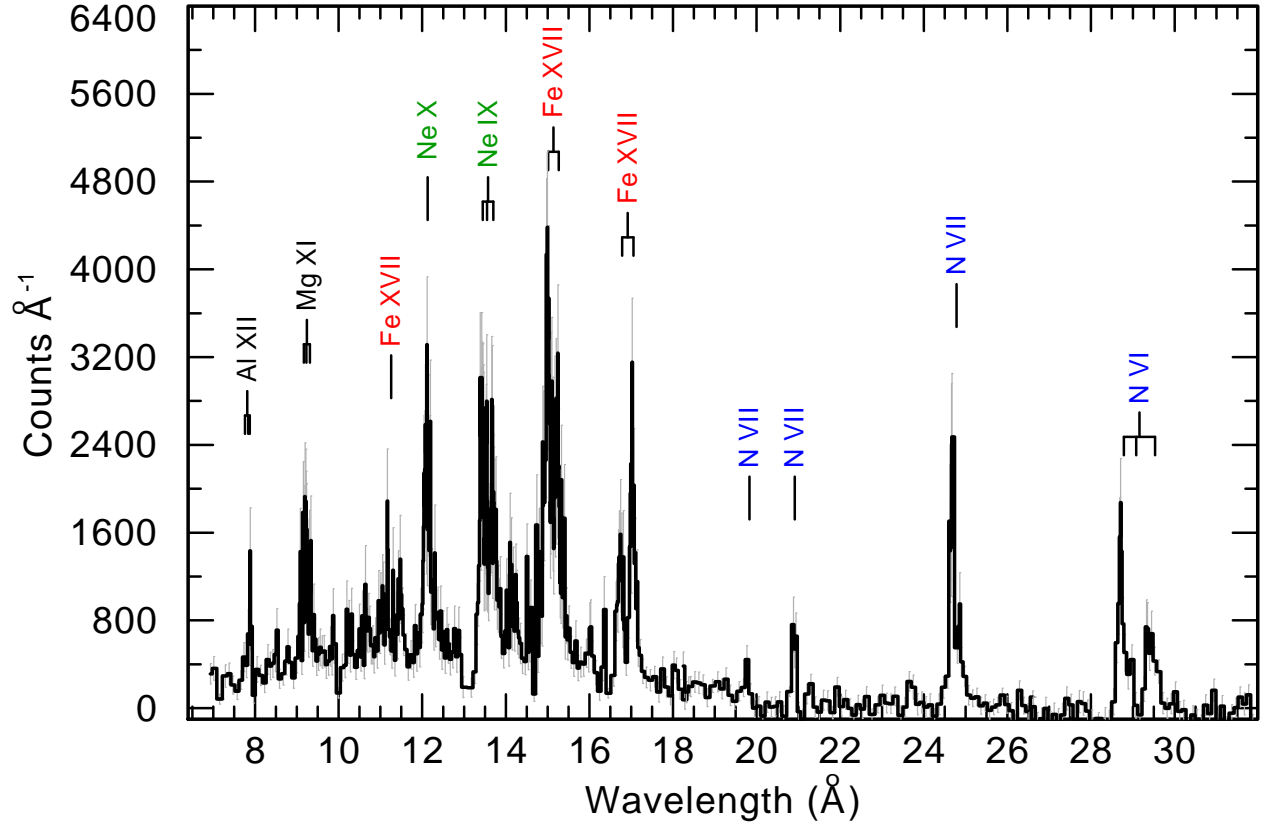


Fig. 1.— The RGS spectrum of WR 6 with the strongest emission lines identified. The error bars correspond  $3\sigma$ . The RGS1 spectrum is shown from 18.2  $\text{\AA}$  to 26.7  $\text{\AA}$ , otherwise the RGS2 spectrum is plotted

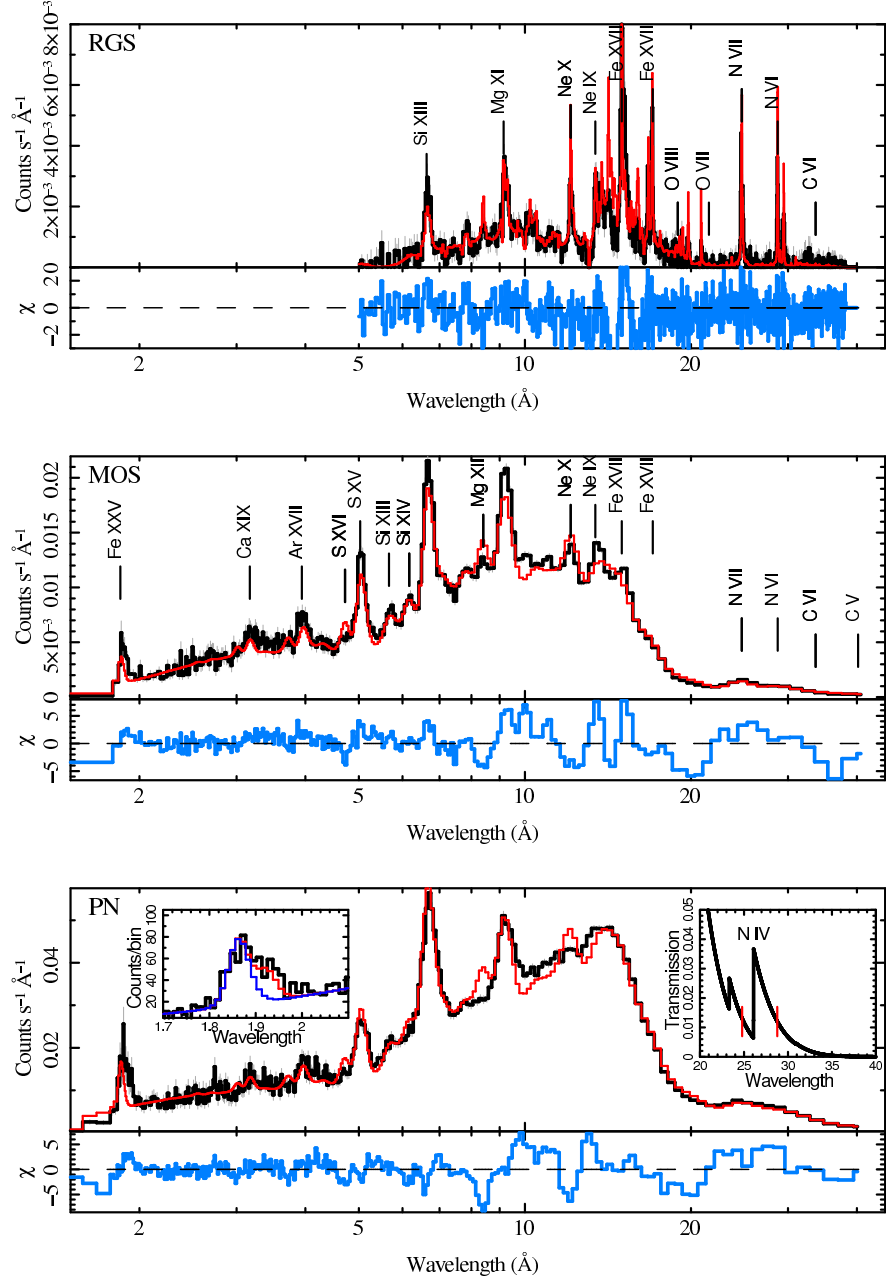


Fig. 2.— The X-ray spectrum of WR 6, obtained with different detectors: RGS (top panel), MOS (middle), and PN (bottom). Black curves display the observations; the model is shown in red. The lower part of each panel displays the residuals. The PN panel includes an inset to the right showing the transmission of the cool wind plus interstellar absorption for  $\lambda > 20 \text{ \AA}$ . The N IV K-shell absorption edge is located between the N VI and N VII lines (red vertical bars). An insert to the left in the PN panel shows a broad spectral feature that is not reproduced by the thermal plasma model (blue dotted line). An additional line at  $1.92 \text{ \AA}$ , which we identify as fluorescent Fe K $\alpha$ , improves the fit (red histogram).

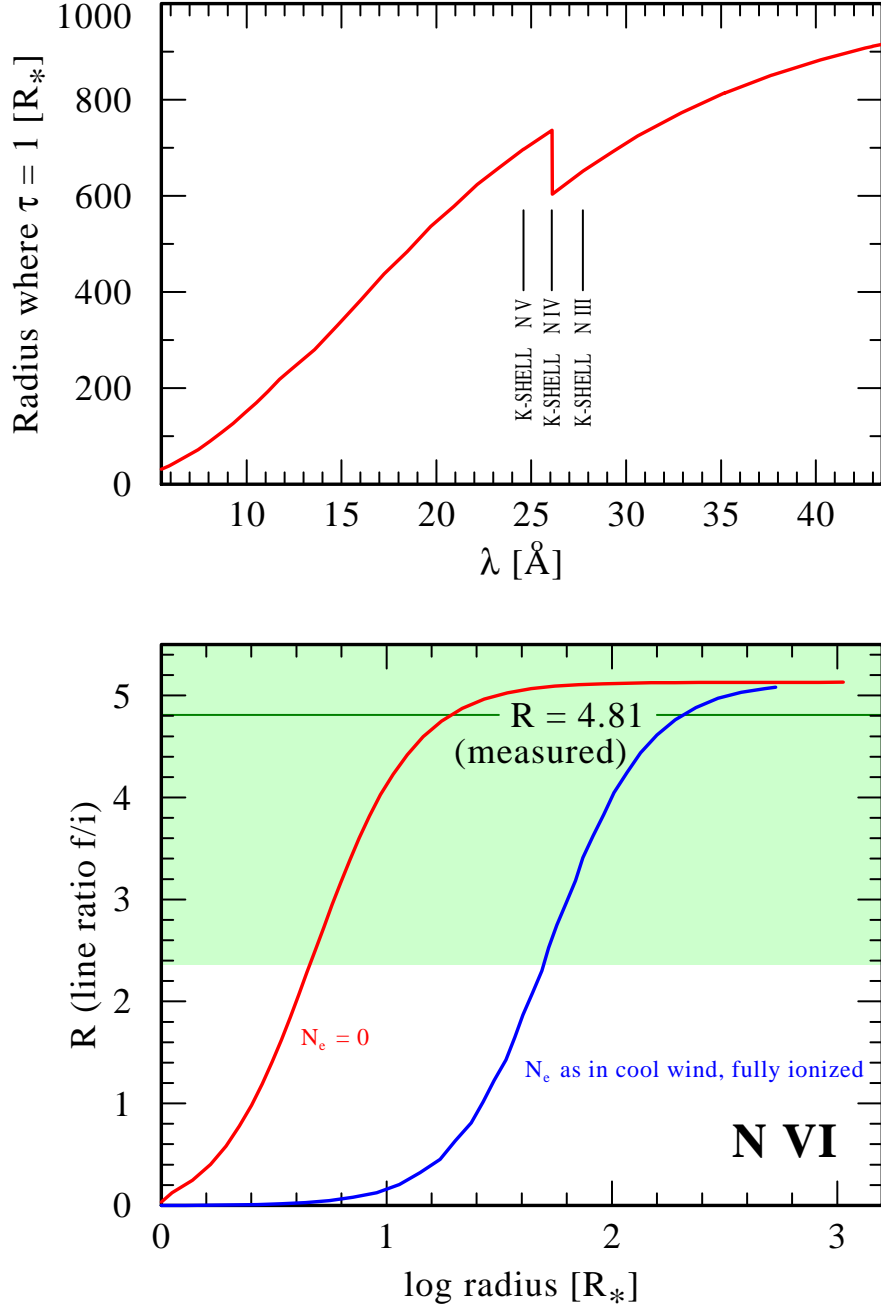


Fig. 3.— *Upper panel:* radius where the continuum optical depth reaches unity, as predicted by the PoWR model for the “cool” wind component of WR 6, when inhomogeneities are only accounted for in the “microclumping” approximation. *Lower panel:* Dependence of the line ratio  $R = f/i$  for the N VI lines as a function of the radial location of the emitting plasma. Based on the PoWR model, the red curve accounts only for radiative de-population, while the blue curve includes also collisional process under the assumption that the shocked plasma has the same density as the cool wind. The measured value is shown as horizontal green line, with the green shaded area representing the  $3\sigma$  confidence band of the measurement.

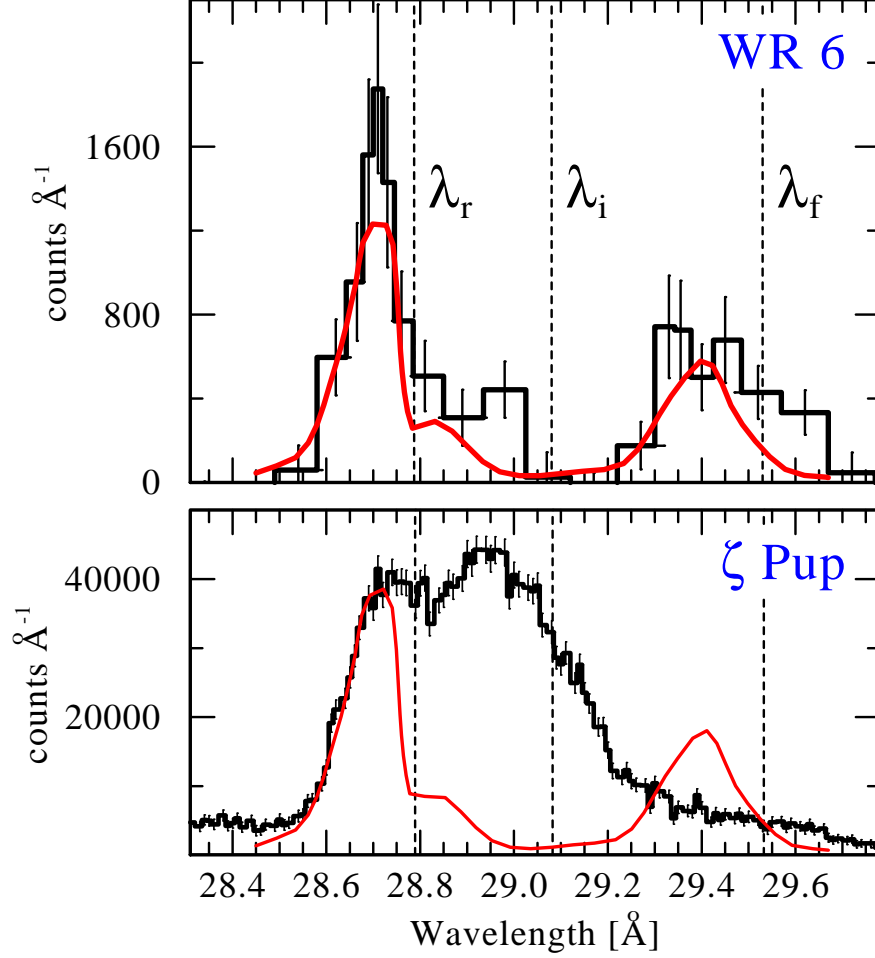


Fig. 4.— *Upper panel:* RGS spectrum of WR6 in the range of the NVI triplet of lines (black). The vertical error bars correspond to  $3\sigma$ . The vertical lines indicate the restframe wavelength of the resonance ( $\lambda_r$ ), intercombination ( $\lambda_i$ ), and forbidden ( $\lambda_f$ ) line, respectively. The solid red line shows a fit to these lines by a formal model with three Gaussian profiles. *Lower panel:* Same as upper, but for the O4I star  $\zeta$  Puppis. The red line shows the scaled Gaussian fit from the upper panel.

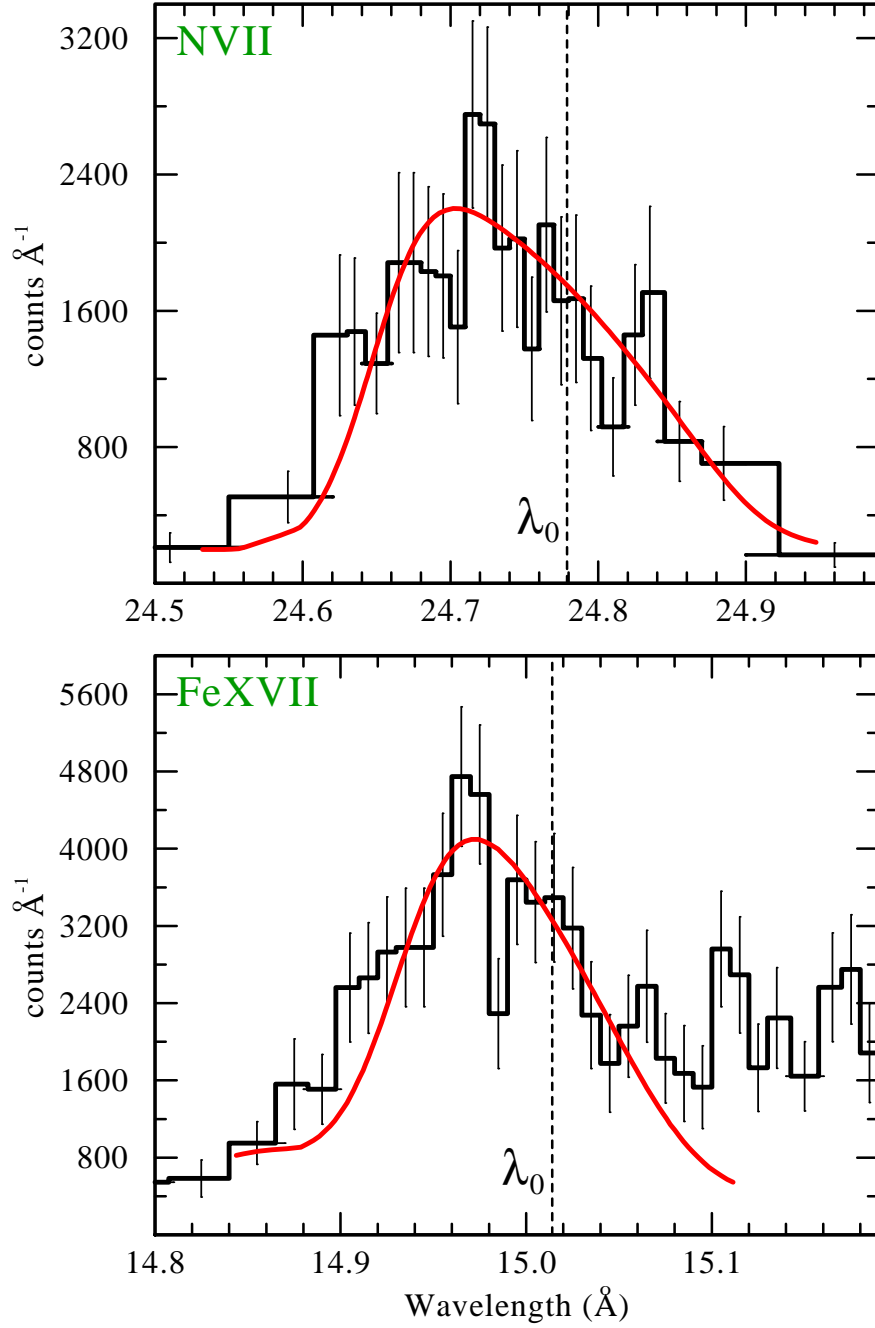


Fig. 5.— *Upper panel:* Part of the spectrum of WR6 centered on the N VII Ly $\alpha$  line. The observed spectrum is shown as a histogram (black). The laboratory wavelength ( $\lambda_0$ ) of N VII Ly $\alpha$   $\lambda$  24.779 Å is indicated by a vertical dashed line. The model line (smooth red) is a blend of N VII Ly $\alpha$   $\lambda$  24.779 Å and  $\lambda$  24.785 Å with a ratio of line emissivities 1 : 0.5. *Lower panel:* The same as upper panel, but for Fe XVII  $\lambda$  15.014 Å. The laboratory wavelength ( $\lambda_0 = 15.014$  Å) is indicated by a dashed line. The model line (smooth red) is a blend of Fe XVII  $\lambda$  15.014 Å and  $\lambda$  14.892 Å with a ratio of line emissivities 1 : 0.1.